



TiO₂/WO₃/Au nanoarchitectures' photocatalytic activity, "from degradation intermediates to catalysts' structural peculiarities", Part I: Aeroxide P25 based composites



G. Kovács^{a,b,1}, L. Baia^{a,c,1}, A. Vulpoi^{a,c}, T. Radu^{a,c}, É. Karácsonyi^d, A. Dombi^d, K. Hernádi^d, V. Danciu^b, S. Simon^{a,c}, Zs. Pap^{a,b,d,*}

^a Faculty of Physics, Babeş-Bolyai University, M. Kogălniceanu 1, RO-400084 Cluj-Napoca, Romania

^b Faculty of Chemistry and Chemical Engineering, Babeş-Bolyai University, Arany János 11, RO-400028 Cluj-Napoca, Romania

^c Institute for Interdisciplinary Research on Bio-Nano-Sciences, Treboniu Laurian 42, RO-400271 Cluj-Napoca, Romania

^d Research Group of Environmental Chemistry, Institute of Chemistry, University of Szeged, Tisza Lajos krt. 103, HU-6720 Szeged, Hungary

ARTICLE INFO

Article history:

Received 1 July 2013

Received in revised form

14 September 2013

Accepted 16 September 2013

Available online 25 September 2013

Keywords:

Aeroxide P25

Tungsten(VI) oxide

Gold nanoparticles

Phenol

UV photodegradation intermediates

ABSTRACT

The "build-up" methodology of a composite photocatalyst is a critical issue regarding the showed photocatalytic performance, including the formation of intermediates. To investigate this issue P25/WO₃/Au composites were obtained by impregnation (WO₃) and subsequent photoreduction (Au) with UV or visible light. The obtained composites' photocatalytic activity and intermediate formation profiles were evaluated using phenol as a model pollutant. XPS/UPS and DRS methods were used to uncover local coordination, surface chemistry (of the different types of atoms (Ti, W, O and Au) and the band-structure (band-gap, possible electron transitions) of the obtained nanomaterials. The intermediates' evolution profile and structural peculiarities were successfully correlated and it was shown that each minor structural (bulk or surface) change has a significant impact on the photocatalytic activity and intermediate formation dynamics.

© 2013 Elsevier B.V. All rights reserved.

1. Introduction

The unfolding story of TiO₂ began in '70s with solar energy conversion and then was continued with photocatalysis which resulted in the manufacturing of several important applications such as self-cleaning and antifogging surfaces. TiO₂ has been the favorite photocatalytic material due to its physical, chemical and commercial merits. But, like everything in the balanced nature, it also has its own insufficiency, the most representative is the wide band-gap energy, which only allows absorption of the UV light of the solar spectrum [1]. Thus, in the last decade a large number of publications appeared concerning coupled semiconductors, especially with TiO₂ which were applied in organic pollutant degradation (photocatalysis) [2–4], catalytic applications [5–7], sensors [8,9] and photocatalytic hydrogen production [10,11]. Among the metal-oxide composites which were reported to be used in the

applications mentioned above were: TiO₂–SnO₂ [12,13], TiO₂–ZnO [14,15] and TiO₂–WO₃ [16,17].

The mixed oxide system formed by TiO₂ and WO₃ has been gained relatively high attention in the literature related to the enhancement of photocatalytic response to UV (absorbed by TiO₂ up to 380 nm, in the case of anatase) and visible light (absorbed by WO₃ up to 480 nm) as well. The increased efficiency of these materials are attributed to the following charge transfer process: photogenerated electrons from TiO₂ are transferred into the lower-energy conduction band of WO₃, whereas the generated holes in the valence band of WO₃ are moved into the higher-energy valence band of TiO₂ [18]. In this way an efficient charge separation is assured, while visible light harvesting is made possible.

Other approach in improvement of the photocatalytic activity of TiO₂ is the deposition of noble metal nanoparticles on the semiconductor surface, catalyzing in this way the interfacial charge transfer process [19]. Among noble metals, the use of gold nanoparticles has got considerable attention in the enhancement of photocatalytic activity of TiO₂, gaining high interest for its results in water-splitting and organic compound-degradations [20]. The usual methods for the modification of TiO₂ with noble metals are the impregnation [21,22] and the photodeposition, the second

* Corresponding author. Tel.: +40 264 593833; +36 62 544338.

E-mail addresses: k.pap.zsolt@gmail.com, pzsolt@chem.u-szeged.hu (Zs. Pap).

¹ First authors.

technique reporting to yield more active photocatalysts [23]. Photodeposition process involves the reduction of noble metal ions by the conduction band electrons, and the water oxidation by valence-band holes [20]. Some organic hole scavengers such as acetate or oxalic acid was added before starting of the process to improve the rate of gold photodeposition [24].

Although both approaches presented above have shown promising results for the enhancement of the TiO_2 photocatalytic performances, to our best knowledge the merging of the two approaches was not studied before. Furthermore, the number of studies regarding the photodegradation intermediates' evolution profile is sparse. This aspect is critical, because it can occur that one of the resulting by-products of the degradation is more toxic than the starting compound, as in the case of phenol.

Phenol and phenolic compounds are widely used in many industries, being one of the most pollutant class of organic materials which are often found in wastewaters. Among other wastewater treatment methods, heterogeneous photocatalysis can be used to eliminate these kind of organic compounds [25,26]. On the other side, during the photodegradation process of phenol, the appearance, in different proportions, of the hydroxylated phenol compounds such as hydrochinon, pyrocatechol and resorcinol was observed [27]. Some of these phenol intermediates are in the category 1 or 2 carcinogenetic risk and aquatic toxicity (according to Regulation (EC) No 1272/2008 [EU-GHS/CLP]). Having different toxicity levels, is crucial to adjust the structure of the photocatalyst in such a way, that the least toxic intermediate formation to be favored.

The main aim of this work was not just to investigate the impact of UV–VIS photodeposition of Au nanoparticles, on the crystallization/crystal phase of TiO_2/WO_3 –Au but also to corroborate their morpho-structural characteristics with the photocatalytic activity of these nanocomposites. Furthermore, another goal of this study was to follow the evolution of the intermediates' concentrations during the phenol photooxidation in order to elucidate the link between them and the structural peculiarities of the obtained nanoarchitectures.

2. Experimental section

2.1. Synthesis of the composites

All chemicals used in synthesis of the composites were of analytical grade (from Sigma-Aldrich) and were used without further purification. 0.78 g (or 0.10 g in the case of the catalysts with 4 wt% WO_3) of H_2WO_4 (as WO_3 precursor) was added to 150 mL 6.6 wt% NH_3 aqueous solution, under stirring at room temperature. 2.27 g of TiO_2 (Evonik Aerioxide P25) was transferred in the obtained solution with continuous stirring at 60 °C for 30 min. The obtained composite was dried in an oven at 80 °C for 24 h and calcined at 700 °C in a muffle furnace (heating rate 4 °C/min), for 2 h in still-air.

The gold deposition was performed under UV light (6 × 6 W Black Light Lamps, with $\lambda_{\text{max}} \approx 365$ nm) using 12 mM HAuCl_4 solution as gold precursor and 50 mM oxalic acid as hole scavenger, in a thermostated 200 mL Pyrex reactor (filled with 175 mL suspension). The P25/ WO_3 catalyst concentration was 1 g/L, while the gold precursor quantity was calculated to have an equivalent of 1 wt% Au on the suspended composite. The reduction process was performed for 4 h. The visible light deposition followed the procedure detailed previously, the only difference was that 6 × 6 W Philips fluorescent lamps (visible light emitting coating) were used and 1 M NaNO_2 was circulated in the thermostating jacket to eliminate any UV radiations. All the composites were washed several times in deionized water and dried at 80 °C for 24 h. Au content was proven

to be ≈ 1 wt% in all the composite materials and no traces of the precursor was detected using UV–Vis spectrophotometry.

2.2. Methods and instrumentation

2.2.1. Characterization methods

X-ray diffraction (XRD) measurements were performed on a *Shimadzu 6000* diffractometer using $\text{Cu}-K_{\alpha}$ radiation ($\lambda = 1.5406 \text{ \AA}$), equipped with a graphite monochromator. The anatase–rutile phase ratio in P25 was evaluated using the Banfield' method [28], and the crystallites average size was calculated using the Scherrer equation [29].

The FT-Raman spectra were recorded by using a *Bruker Equinox 55* spectrometer with an integrated *FRA 106 Raman* module using an Nd-YAG laser (1064 nm). Raman spectra were recorded with a spectral resolution of 1 cm^{-1} .

JASCO-V650 spectrophotometer with an integration sphere (*ILV-724*) was used for measuring the *DRS spectra* of the samples ($\lambda = 300$ –800 nm). To obtain the band-gap energy the reflectance data were converted to $F(R)$ values according to the Kubelka–Munk theory. The band gap was obtained from the plot of $[F(R) E]^{1/2}$ versus energy of the exciting light (E). The possible electron transitions were evaluated by plotting the $dR/d\lambda$ vs. λ , where R is the reflectance and λ is the wavelength.

FEI Quanta 3D FEG dual beam-in high vacuum mode using EDT (Everhart Thornley Detector) electron microscope (equipped with an Apollo-X SDD Energy Dispersive X-ray (EDX) detector) was used to obtain quantitative elemental analyses (i.e. gold content). TEM images were obtained with a *Jeol JEM 1010 TEM* operating at an accelerating voltage of 100 kV and equipped with a *MegaView III* CCD camera (Fig. 1)

XPS measurements were performed on a *SPECS PHOIBOS 150 MCD* instrument, with monochromatized $\text{Al } K_{\alpha}$ radiation (1486.69 eV) at 14 kV and 20 mA, and a pressure lower than 10^{-9} mbar. Samples were mounted on the sample holder using double-sided adhesive carbon tape. High-resolution $\text{Au}4\text{f}$, $\text{Ti}2\text{p}$, and $\text{W}4\text{f}$ spectra were recorded in steps of 0.05 eV for the analyzed samples. Analysis of the obtained data was carried out with *CasaXPS* software. All peaks have been deconvoluted using Shirley background and Lorentzian–Gaussian line shapes. The applied value of the Gaussian–Lorentzian ratio was 30.

Microprocessor controlled surface area analyzer, *Qsurf Series M1*, was used for the N_2 adsorption measurements. Outgassing at 200 °C was performed for 30 min, to ensure maximum accuracy of the obtained information. The specific surface area of the composites was evaluated on the basis of Brunauer, Emmet and Teller (B.E.T.) equation.

$^{13}\text{C-NMR}$ spectra were recorded by using the *Bruker AVANCE 400* spectrometer, a spinning speed of 10 kHz and the cross polarization technique. As reference for the chemical shift tetramethylsilane was used.

2.2.2. The assessment of the photocatalytic efficiencies and the normalization of the activities

A photoreactor system with 3 *LighTech 40 W* fluorescent lamps ($\lambda_{\text{max}} \approx 365$ nm, irradiation distance = 5 cm, irradiation time = 3 h) was used to measure the photocatalytic activities. The photocatalyst suspension containing phenol (initial concentration of phenol $c_{0,\text{phenol}} = 0.5 \text{ mM}$; catalyst concentration $c_{\text{suspension}} = 50 \text{ mg}/50 \text{ mL} = 1.0 \text{ g/L}$; total volume of the suspension $V_{\text{susp}} = 50 \text{ mL}$) was continuously purged by air in order to maintain the dissolved oxygen concentration constant during the whole experiment. The concentration decrease of the chosen organic substrate (phenol) and their degradation intermediates were followed using an *Agilent 1100 series HPLC* system (Fig. S1). The assessed error

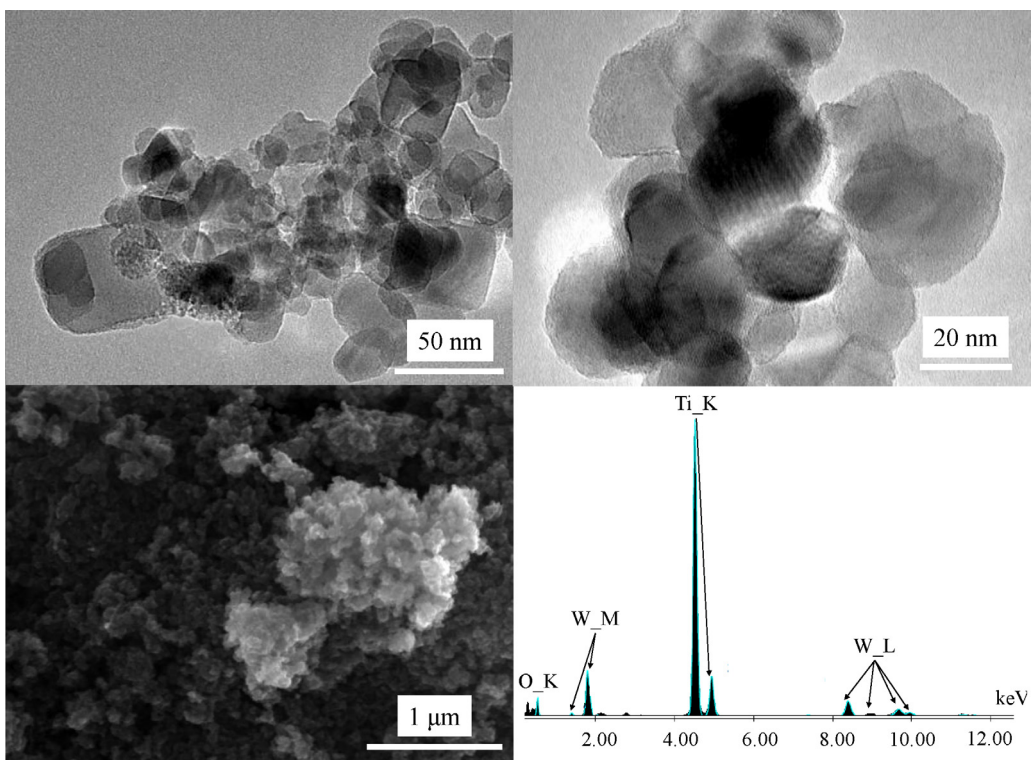


Fig. 1. SEM/TEM micrographs and EDX spectrum of sample P25/WO₃(24%).

of the photocatalytic tests (based on reproducibility experiments) was 5–9%.

To quantify the intermediates' evolution an intermediate evolution index (IEI) was calculated, using the formula:

$$\text{IEI} = \left| \int_0^{C_{\text{phenoldef}}} F_{\text{int}} dC \right|$$

In the equation above F_{int} is the empirical intermediate concentration evolution function, $C_{\text{phenoldef}}$ is the quantity of phenol degraded in the case of the less performing catalyst (0.15 mM phenol consumption in the present case). A low IEI value means that the degradation intermediate does not accumulate in the reaction system. The error limits of this evaluation method was estimated to be $\pm 2\text{--}5\%$.

The obtained reaction rates were normalized to the surface area of the photocatalysts to emphasize the surface quality's critical importance. These normalized data are in strong relationship with the surface structural data, which will provided for each of the materials obtained. The normalization took place as follows:

$$r_{\text{normalized}} \left(\frac{\text{mM} \times \text{g}}{\text{m}^2 \times \text{h}} \right) = \frac{r \left(\text{mM} \times \text{min}^{-1} \right)}{S_{\text{BET}} \left(\text{m}^2 \times \text{g}^{-1} \right)} \times 60$$

3. Results and discussions

3.1. The photocatalytic activity of the obtained nanocomposites at phenol degradation

Although, the usual discussion in the papers regarding similar subjects begins with the characterization of the photocatalysts, in this case it is not adequate because the succession of the research results could become ambiguous. Consequently, the photocatalytic activity is presented in the first instance.

Our previous experiments regarding gold deposited titanias [27] showed that the gold presence inhibited the phenol (poorly adsorbing substrate) decomposition rate both under UV and visible light, while the degradation rates increased for oxalic acid (good adsorption properties). Fortunately, and in the same time the obtained nanomaterials were competitive in degradation rate terms, with the well-known Evonik Aerioxide P25 (Fig. 2). The best performing sample was the P25/WO₃(4%)–Au–UV, achieving 95% of the P25's activity (Table 1). This situation was overturned when the reaction rates were normalized to the specific surface area, namely P25/WO₃(4%)–Au–UV became with 17% more active than the previously mentioned P25 (Table 1).

In the case of sample P25/WO₃(24%)–Au–UV, the most intriguing effect was that the gold presence increased the phenol

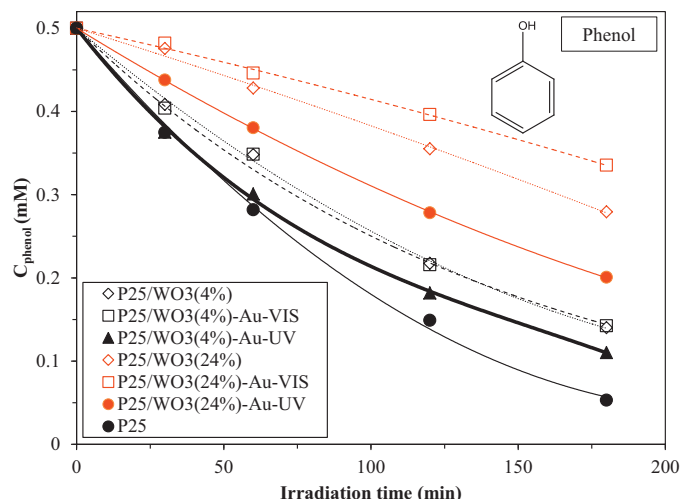


Fig. 2. Phenol degradation curves of the prepared nanocomposites.

decomposition rates twice (from 1.1 to 2.18 $\mu\text{M}/\text{min}$). Furthermore, a difference in the activity was observed when the gold was deposited under visible or UV light. Interestingly, visible light deposited titanias were less active, while the UV deposited

composites were twice more efficient than their appropriate starting materials (i.e. P25/WO₃(24%)) (Table 1).

The results shown above raise questions related to the photocatalytic behavior of the investigated samples, as long as no precise

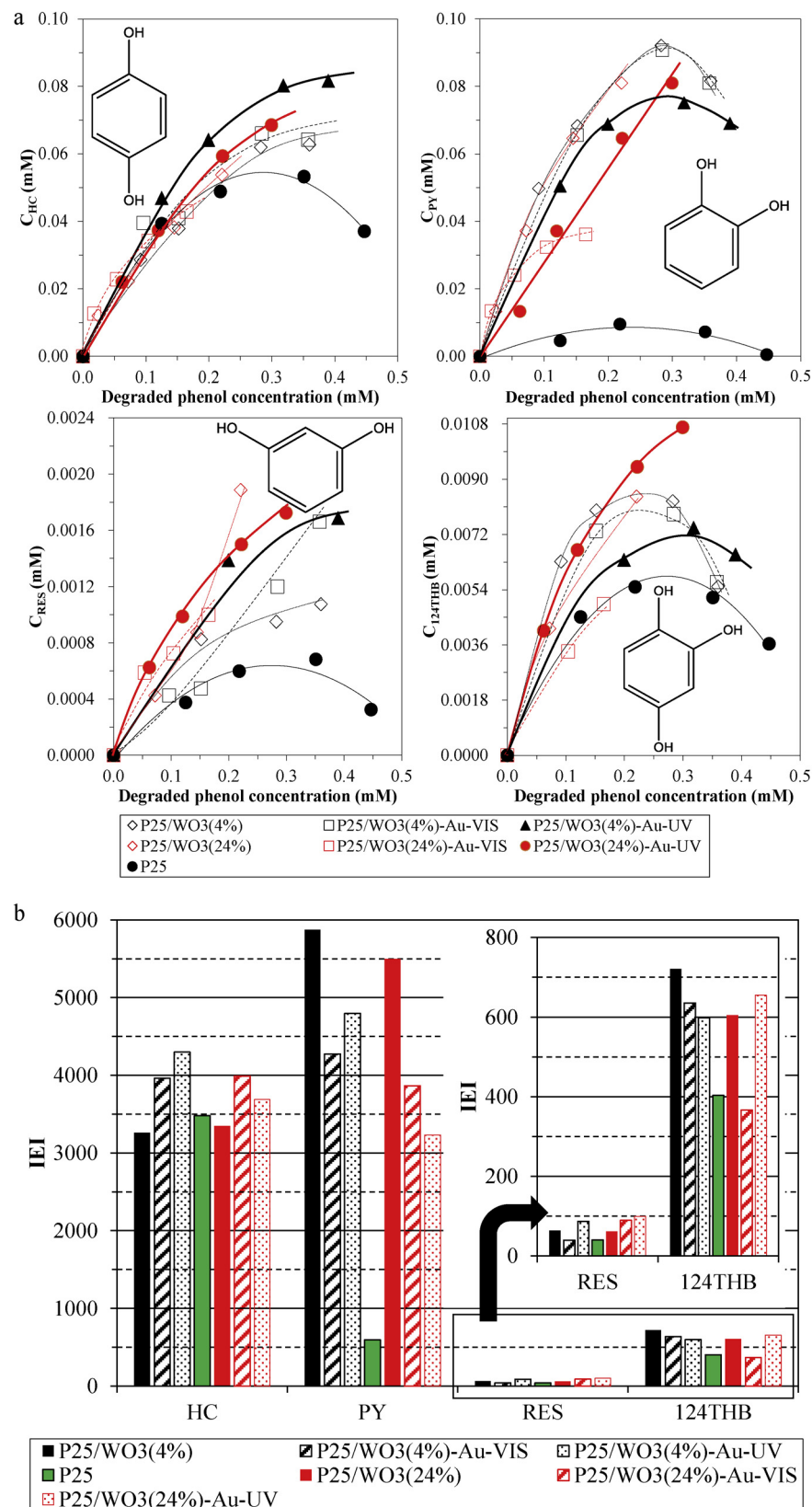


Fig. 3. (a) Phenol degradation intermediates' concentration profile. (b) Phenol UV photodegradation intermediates' IEI values compared among the P25 based composites.

Table 1

Phenol UV photodegradation rates, significant structural parameters and IEI values of the obtained nanocomposites.

Sample name	Phenol degradation rate ($\mu\text{M}/\text{min}$)	S_{BET} (m^2/g)	Normalized phenol degradation rates ($\text{mM}/\text{h} \times \text{m}^{-2}$)	Crystallites mean size (nm)		Intermediate evolution index (IEI)			
				TiO ₂		WO ₃	HC	PY	RES
				Anatase/rutile	Monoclinic				124THB
P25/WO ₃ (4%)	2.98	33.8	5.29	32/48	–	3262	5873	63.67	721.0
P25/WO ₃ (4%)–Au–VIS	3.04	39.6	4.61	30/46	–	3962	4275	39.53	635.4
P25/WO ₃ (4%)–Au–UV	3.92	39.5	5.95	30/46	–	4299	4797	86.93	597.8
P25	4.12	50.0	4.94	25/40	–	3480	595	40.07	403.2
P25/WO ₃ (24%)	1.10	69.1	0.95	31/43	22	3348	5499	61.27	604.7
P25/WO ₃ (24%)–Au–VIS	0.78	69.6	0.67	32/44	24	3990	3865	89.20	366.4
P25/WO ₃ (24%)–Au–UV	2.18	36.9	3.54	34/50	25	3687	3232	99.23	655.2

information can be found in the literature regarding this aspect. Having in mind that the intermediates can cause serious toxicity problem in real cases, their appearance from the structural peculiarities perspective is a critical issue from the photocatalysts' applicability point of view.

3.2. Phenol degradation intermediates—Fig. 3a and b

The present section will “take under the loupe” the evolution of the hydrochinon (HY), pyrocatechol (PY), resorcinol (RES) and 1,2,4-trihydroxy-benzene (124THB) concentrations in the frame of the composite build-up. The main influence possibilities will be enumerated later on in direct relation with the structural peculiarities. All the specific IEI values can be found in Table 1.

Three aspects can be efficiently followed by the careful examination of the intermediates. The first one is the effect of the WO₃ addition/appearance in the composite system. In this case the appropriate reference is P25. Comparatively, both P25/WO₃(4%) and P25/WO₃(24%) had a slightly smaller intermediate evolution index (IEI) of HC. Ten times higher IEI values were registered for PY, while “only” a $1.5 \times$ increase for RES and 124THB was observed. It means that the presence of WO₃ favors the formation of PY, RES and 124THB. This distribution of the intermediates was altered for the gold containing composites (both UV and visible light deposited).

In the case of the photodeposition of gold nanoparticles using UV light the appropriate references were P25/WO₃(4%) and P25/WO₃(24%). An IEI increase for HC and RES, together with PY IEI value decrease was noticed, while unbalanced (meaning an unclear influence) 124THB IEI values were registered. The listed values indicated in Table 1 clearly points out that UV gold deposition influences differently the degradation intermediates concentration profile, depending on the WO₃ quantity.

The gold nanoparticles' deposition was also realized using visible light ($\lambda > 400$ nm). As expected, just by changing the wavelength of the deposition, the obtained ternary composites showed different photocatalytic activity and intermediate concentration profiles. An increase of the IEI value for HC, a decrease of IEI value for PY and 124THB while unbalanced values were recorded for RES.

As shown above, by changing selected structural aspects of the composites a significant intermediate evolution profile changes (quantified in IEI values) were observed. Consequently, an in-detail investigation was necessary to elucidate which structural entity is responsible for the mentioned changes.

3.3. Structural/optical aspects of the TiO₂/WO₃/Au composites

3.3.1. X-ray diffraction (XRD)—Crystal phase composition and particle size

The TiO₂ component being the well-known commercial Evonik Aeroxide P25, there are no surprises regarding the crystal phase

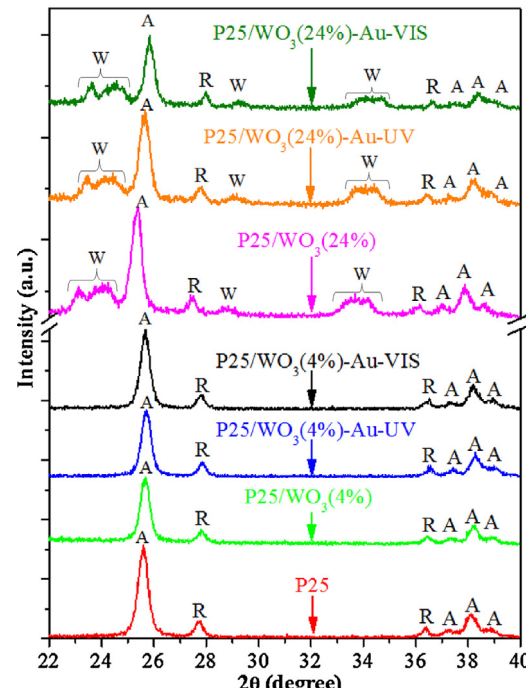


Fig. 4. XRD patterns of all the studied nanocomposites (W = tungsten oxide (monoclinic), A = anatase, R = rutile).

composition (89 wt% anatase, 11 wt% rutile–bare Aeroxide P25) and crystallites' mean size (25 nm anatase and 45 nm rutile–bare Aeroxide P25) (Fig. 4). Although the composites (before gold deposition) were heat treated at 700 °C, no changes were observed in the anatase/rutile ratio and only a small variation was observed in their particle size (Table 1). The 1 wt% gold content was not detectable due to the low gold content and due to the fact that the main diffraction peaks were covered by the diffraction patterns of the semiconductors [17]. Furthermore, as expected, these nanoparticles did not influence the bulk crystalline structure of the semiconductors. However, an interesting feature was observed in the diffraction data of P25/WO₃(24%)–Au–UV (Fig. S2). After the catalyst washing/drying step the dried powder contained three differently colored phases. Among them it was found a TiO₂ and a WO₃ dominant phase. In the titania dominant phase a robust deformation of the (112) anatase peak was observable. This deformation occurs exactly where the (111) gold peak is usually found, meaning that the gold deposition under UV light mainly occurred mainly on the titania phase, causing in the same time a separation of WO₃ rich phase. This phenomena needs further in-detail investigations.

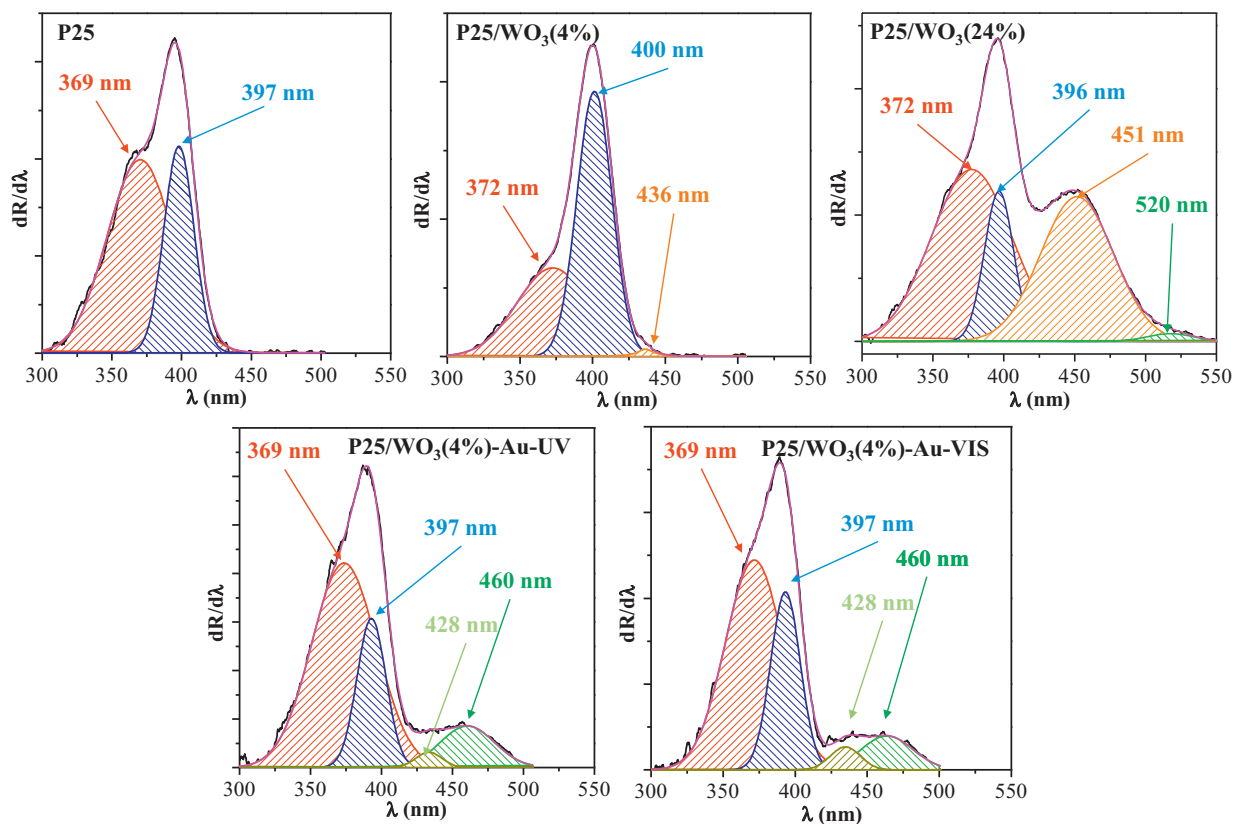


Fig. 5. First order derivatives of the DRS spectra obtained for 5 selected samples.

The WO_3 related diffraction peaks appear only in the case of the samples containing 24 wt% tungsten(VI) oxide and they indicate a monoclinic crystalline structure with a 22–25 nm crystallite size. In the first instance, the most plausible explanation is that the used instrument's sensitivity is not enough to detect 4 wt% WO_3 . Consequently, the mentioned diffraction patterns were re-recorded, with a twofold sensitivity. The newly obtained diffraction patterns still did not show any sign of WO_3 . This observation means that the WO_x species, originating from the precursor doped the TiO_2 component or they are present as amorphous islands. To prove this, the optical properties and the crystallinity related aspects of the composites were explored by DRS and Raman spectroscopy.

3.3.2. Diffuse reflectance spectroscopy (DRS)—Optical properties

P25 itself is a white powder, meaning that this material absorbs mostly UV light. If the DRS spectrum of this composite is analyzed, than two electronic transitions are observable, which could be responsible for the mentioned UV light absorption. One of them is at ≈ 370 nm and the other one at ≈ 397 nm, which in terms of energy correspond to the band-gap value of anatase and rutile. If the materials' structure changes (by doping), than, at least, a change in the ratio of these peaks should be observable. This was the case of the previously mentioned samples containing 4 wt% WO_3 , where no specific WO_3 phase was present. Indeed, as it is shown in Fig. 5 the ratio of the two bands are changed, indicating the high probability of tungsten doping. Furthermore, in the case of the composite containing 24 wt% WO_3 , the ratio of the two titania transition bands remains intact, while new bands appear (at 451 and 520 nm) in the visible region, which can be attributed to the presence of WO_3 .

Furthermore, the gold deposition also induced clear changes to the possible electronic transitions. Namely, in the case of samples P25/WO₃(4%)-Au-UV and P25/WO₃(4%)-Au-VIS, the band at

369 nm becomes more intense than the signal recorded at 397 nm in the case of UV gold deposited sample, making possible a greater number of electronic transitions in the UV region, as shown in Fig. 5, while in the case of the visible light deposited gold containing composite, this difference is quiet small.

The same behavior was observed also in the case of the 24 wt% WO_3 containing composites with gold. Additionally, the DRS spectra revealed the asymmetry of the plasmonic band towards higher wavelengths that denotes the increase of the Au aggregated nanoparticle's number [30,31]. Thus, it can be inferred that the samples prepared under visible light irradiation give rise to a higher amount of isolated gold nanoparticles compared with those prepared under UV irradiation. In all cases the gold nanoparticles' average size was ~ 50 nm.

3.3.3. The WO_3 and TiO_2 's crystallinity related aspects—Raman spectroscopy

From the DRS spectra it seems, that the WO_3 is present as individual particles in the case of the composites which contained 24 wt% of tungsten oxide, while in the case of low WO_3 concentration (4 wt%) a W doping occurs. However, based on this method it is not clear that whether there are any other WO_3 "forms" (i.e. amorphous WO_3) in the composites. For this Raman spectroscopy was performed on the obtained composites.

The FT-Raman spectra shown in Fig. 6 reveal the presence of the bands characteristic for TiO_2 anatase and rutile phases (very weak) located around 144, 197, 394, 512, 638 and 455 cm^{-1} , respectively [32,33].

The WO_3 crystalline structure (monoclinic) generally gives rise to characteristic Raman bands around 710 and 800 cm^{-1} , while the amorphous species are indicated by the ones centered at ≈ 260 cm^{-1} (O–W–O bending modes), 950–960 cm^{-1} (W=O

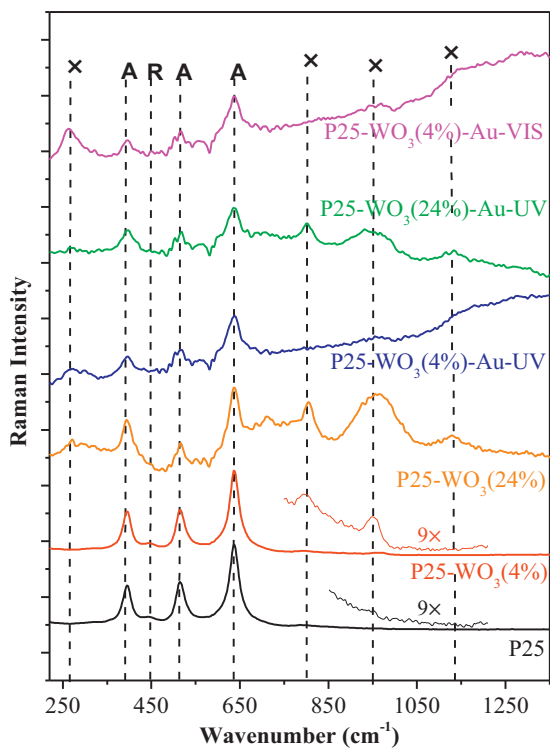


Fig. 6. Raman spectra of investigated photocatalysts (sample P25/WO₃(24%)-Au-VIS is not presented here due to the excessive interference of gold). (In the case of sample P25 and P25/WO₃(4%) a 9 factor zoom was also provided).

stretching) and 1126 cm⁻¹. This means that on all the 4 wt% WO₃ containing samples' surface, WO₃ can be found in an amorphous (950 cm⁻¹) phase, whose existence was also proved by Akurati et al. [34]. Additionally, according to the DRS data, tungsten doped TiO₂ structures are also present in these samples. In the case of P25/WO₃(24%) catalysts, both crystalline (bands at 710 and 800 cm⁻¹) and amorphous WO₃ (bands located at 260, 950 and 1126 cm⁻¹) were found. Unfortunately, by analyzing the spectra it was observed a considerable increase of the Raman background once the gold photodeposition was performed. This signal occurs due to the intense backscattered light recorded and made extremely difficult any detailed discussion.

The information gathered until this point shows that the WO₃ is found under several forms (as dopant, amorphous and separate crystalline particles-depending on the synthesis conditions) attached to TiO₂. Since the photocatalytic processes are directly surface quality related it is crucial to understand the surface chemistry of these materials, and therefore, XPS and UPS techniques were further applied to enlighten this aspect.

3.3.4. The surface chemistry of the TiO₂/WO₃-Au composites (Fig. 7)

Three major elements were followed during this investigation, namely the W, Ti and Au. In the case of gold the width of the 4f lines (FWHM) of the Au4f spectra for the sample containing 4% WO₃ is similar, while in the samples with 24 wt% WO₃ variations in both, Au4f core level and VB (valence band) spectra is observed and may be associated with the Au atoms distribution on the composite surface [35,36]. This latter observation was reinforced by the DRS spectra.

The Ti2p XPS region can be deconvoluted in three components as follows: the first one 2p1/2, at 464.45 eV, and Ti 2p 3/2 at 458.75 eV

was attributed to Ti⁴⁺ in the bulk TiO₂ [37,38]; the second component at \approx 2 eV lower, with Ti 2p 1/2 at 461.2 eV and Ti2p3/2 at 457.2 eV was assigned to Ti³⁺ [39], while the third Ti2p peak at 459.3–465.4 eV was given by the TiO_x-W entities. The latter one was observed in several mixed oxide systems [40] containing TiO₂ and WO₃. Interestingly, Ti³⁺ was detected only in the samples containing 4 wt% of WO₃, hinting the existence of oxygen vacancies (or low binding energy oxygen atoms [41], not observed here), which usually are a direct consequence of doping (already demonstrated by DRS). Furthermore, the Ti³⁺ concentration is at its highest value in the P25/WO₃(4%) composite (5.9% from the total Ti), meaning that the deposition of gold stabilizes the surface of the catalyst. This effect was intense in the case of P25/WO₃(4%)-Au-VIS sample (1.5% Ti³⁺ from the total Ti), because the gold was homogeneously dispersed on the surface (reinforced by the Au4f XP spectra and the DRS). Furthermore, the TiO_x-W entities in the 24 wt% WO₃ containing composites are three times more abundant (Table 2) than in the ones with 4 wt% WO₃. However, the multiplier should be six instead of three, due to the WO₃ concentration difference. This suggests that the WO₃ is well dispersed in the case of lower WO₃ concentrations.

From fitting the spin orbit doublet of W4f, the one at 35.5/37.6 eV was generated by photoelectrons emitted by W⁶⁺ species (WO₃) [42,43]. The second doublet at 33.7/35.8 eV was attributed to photoelectrons emitted from W atoms near O vacancies in the WO₃ lattice, where the oxidation state of W is +4 [42,43]. A third component at 37.5/39.7 eV was associated to defects (W_{def}) present at the surface of the sample (amorphous zones, prior crystallization/defectively crystallized). Additional components at 37.41 and 41.78 eV were associated to Ti3p level in TiO₂ and W5p [44]. These latter entities were not included in the total W calculation.

The impregnation of P25 with 4 wt% WO₃ resulted doping of TiO₂ lattice (supported by several evidences presented previously), a small fraction of defect crystalline WO₃ (the presence of W⁴⁺) and a fraction of amorphous WO₃ (mostly Raman and XRD supported and partially by W_{def}). As the gold deposition occurred the ratio of the W species' concentration was changed in an interesting way. In both cases (UV and Vis gold deposition) the doubling of the W⁴⁺ concentration (from 5.2% to 10.8% and 10.2%—Table 2) was observed, meaning that the fraction of the crystalline WO₃ entities increased. In the case of P25/WO₃-Au-VIS the W⁴⁺ increased, while W_{def} decreased, meaning that the amorphous matter was crystallized during the gold's visible light deposition. In the case of UV induced Au photodeposition, the W⁴⁺ increased, while nearly no changes were observed in the W_{def} concentration. The formed W⁴⁺ originated from the W⁶⁺, and its decrease of about 5% suggesting the defection of the already crystalline WO₃.

The impregnation of P25 with 24 wt% WO₃ determined the same surface W species (except for W_{def}), meaning that the WO₃ entities are crystalline at the surface (no W_{def} peaks). In this situation also, the W⁴⁺ formed while W⁶⁺ decreased while depositing gold on the surface of the composites, both under UV and visible light. Furthermore, the amorphous WO₃ is probably located in the bulk of the WO₃ particles, because it was observable through Raman spectroscopy.

3.3.5. NMR spectroscopy—Hints about a possible phenol adsorption on WO₃

The comparison of the ¹³C-NMR spectra (Fig. 8) recorded before and after phenol adsorption reveals the occurrence of important changes in the chemical shifts of both carbon sites, the OH linked carbon and the unlinked one. Thus, the signals recorded at 156.1 and 155.6 ppm (157 and 156.5 ppm, respectively, after adsorption) originates from the site where carbon is bonded by OH (position 1 in the benzene ring). The peaks observed at 131.5 and 130.6 ppm

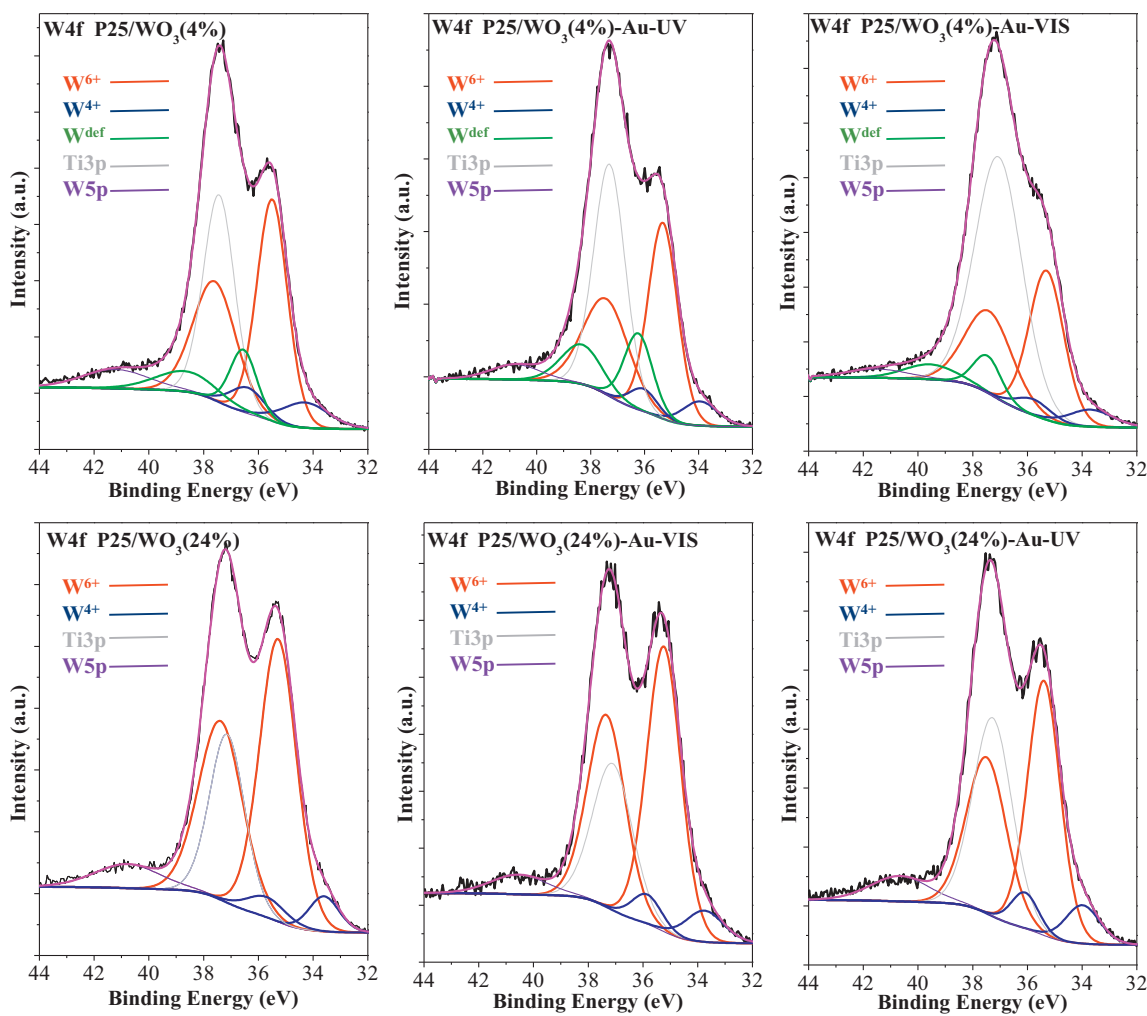


Fig. 7. W4f XPS spectra of all the nanocomposites.

(132.6 and 131.5 ppm, respectively, after adsorption) can be associated with the presence of the two equivalent carbons (positions 2 and 6 in the benzene ring), whereas the signals at 123.1 and 122.1 ppm (124.0 and 123 ppm, respectively, after adsorption) can be attributed to the carbon located in the opposite side relative to the OH bonded carbon. The peaks recorded at 117.4 and 116.3 ppm (118.3 and 117.2 ppm, respectively, after adsorption) is given by other two equivalent carbons (positions 3 and 5 in the benzene ring). Consequently, the observations enumerated above can be considered as a direct evidence of the phenol adsorption process on WO_3 (in the literature it is described that W can form phenolate complexes [45]).

3.4. Linking structural features with activity and intermediate formation

In this section a corroboration of the photodegradation/intermediate compounds' related data with structural characteristics will be presented together with a plausible explanation (where the data correlation will be not clear, just the bare relations will be given).

The addition of tungsten oxide in 4 wt% increased significantly the IEI of the hydroxylated products, and slightly the photocatalytic activity. This increase can be attributed to the appearance of crystal lattice defects in both oxides (Ti^{3+} , W_{def} , W^{4+}). Usually,

Table 2
Representative species and their ratio in the studied nanocomposites.

Sample name	Normalized phenol degradation rates ($\mu\text{M}/\text{h} \times \text{m}^{-2}$)	Representative species detected by XPS				
		Total Ti = 100%		Total W = 100%		
		Ti^{3+} (%)	$\text{TiO}_x\text{-W}$ (%)	W^{6+} (%)	W^{4+} (%)	W_{def} (%)
P25/WO ₃ (4%)	5.29	5.9	11.8	73.2	5.2	22.6
P25/WO ₃ (4%)-Au-VIS	4.61	1.5	16.4	74.1	10.8	15.1
P25/WO ₃ (4%)-Au-UV	5.95	4.4	10.9	65.1	10.2	24.7
P25	4.94	–	–	–	–	–
P25/WO ₃ (24%)	0.95	–	37.1	90.8	9.2	–
P25/WO ₃ (24%)-Au-VIS	0.67	–	34.5	89.1	10.9	–
P25/WO ₃ (24%)-Au-UV	3.54	–	37.6	86.0	14.0	–

Table 3
The quantification of the influence of structural parameters: if a parameter increase raised the IEI value, than the gained value is “+” while in the case of opposite impact (parameter increase, negative influence on the IEI value), the given value is “–”. Additionally, if no “reaction” was noticed in the IEI value during a structural parameter change or vice versa, the influence was considered 0.

Intermediate	Influence scores						Information zone
	a	b	c	d	e	f	
HC	0	+	–	–	–	–	
PY	0	–	+	–	+	+	
RES	0	–	–	+	+	+	
124THB	0	–	–	+	–	+	
Cumulative influence							
Parameter							Crystallinity-XRD
Information zone							Bulk (total influence:12)
							Doping-DRS
							Amorphous WO_3 -Raman

Intermediate	Influence scores						Information zone
	a	b	c	d	e	f	
HC	–	+	–	–	–	–	
PY	–	–	+	–	+	+	
RES	–	–	–	+	+	+	
124THB	–	–	–	+	–	+	
Cumulative influence							
Parameter							Surface area- N_2 adsorption (BET)
Information zone							Ti ³⁺ -XPS
							W ⁶⁺ -XPS
							W ⁴⁺ -XPS

Intermediate	Influence scores						Information zone
	a	b	c	d	e	f	
HC	–	+	–	–	–	–	
PY	–	–	+	–	+	–	
RES	–	–	–	+	+	–	
124THB	–	–	–	+	–	+	
Cumulative influence							
Parameter							Surface (total influence: 26)
Information zone							Ti ³⁺ -XPS
							W ⁶⁺ -XPS
							W ⁴⁺ -XPS

Intermediate	Influence scores						Information zone
	a	b	c	d	e	f	
HC	–	+	–	–	–	–	
PY	–	–	+	–	+	–	
RES	–	–	–	+	+	–	
124THB	–	–	–	+	–	+	
Cumulative influence							
Parameter							Surface area- N_2 adsorption (BET)
Information zone							Ti ³⁺ -XPS
							W ⁶⁺ -XPS
							W ⁴⁺ -XPS

a—The addition of WO_3 in 4 wt%; b—The addition of WO_3 in 24 wt%; c—The UV deposition of gold on 4 wt% WO_3 containing composites; d—The Vis. deposition of gold on 4 wt% WO_3 containing composites.

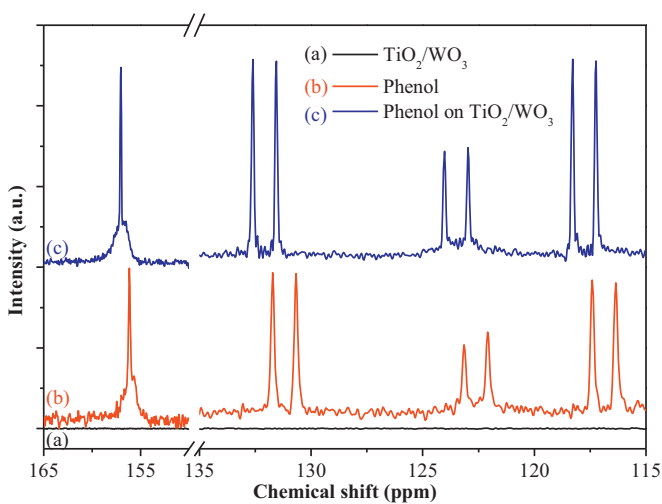


Fig. 8. ^{13}C -NMR spectra of sample P25/WO₃(24%) in the absence/presence of phenol.

they serve as active or as increased adsorption sites [41]. The latter one can be made responsible for the unusually high PY and slightly higher HC concentrations, compared to bare P25, due to the fact that W usually forms phenolate complexes [45], which was indirectly demonstrated in the earlier section. The as-adsorbed phenol can be easily attacked at the 2nd and 4th carbon atom (in ortho and para positions) by the OH radicals, resulting HC and PY.

The gold deposition on the surface of the P25/WO₃(4%) induced interesting changes in the structural features of the material. The W⁴⁺ surface concentration increased significantly, meaning that the gold deposition induced a further crystallization of the amorphous WO_3 . The HC IEI increased, meaning that more successful OH attacks were performed on “fixed” phenol (complexated at the W⁴⁺ sites). In the same time the PY and the THB values decreased, in accordance with the Ti³⁺ concentration (Table 2). This suggests that the defects/doping induced in the titania lattice are responsible for these by-products.

The addition of tungsten oxide in 24 wt% lowered the observed photocatalytic activity, due to the formation of attached WO_3 particles, while the IEI values are comparable, meaning that the rate determining step is the degradation of the hydroxylated by-products. At this tungsten oxide concentration no more W_{def} and Ti³⁺ species can be found, while the other species were more abundant, as expected, due to the higher WO_3 concentration. A single exception was the W⁴⁺ species found in comparable quantities with P25/WO₃(4%), but their number should be higher due to the higher concentration of tungsten oxide. This fact revealed that the WO_3 entities are quiet well dispersed in the P25/WO₃(4%) nanocomposite. As we have already proven [17], the appearance of individual WO_3 particles, at higher WO_3 concentrations (above 10–14 wt%), was unfavorable in the terms of photocatalytic activity. The gold deposition on the surface of the P25/WO₃(24%) induced a higher abundance of W⁴⁺ sites, but not as much as should be. By gold deposition, the HC IEI increased while the PY IEI value decreased (no clear correlations THB). The UV induced gold deposition resulted in a selective photodeposition on the titania particles, resulting an efficient catalyst compared to P25/WO₃(24%) (Table 1, Fig. 2), while in the case of visible light gold deposition an activity inhibition was noticed. In both cases a RES IEI increased, revealed that RES formation is favored by the presence of gold. Unfortunately, the relations discussed above in this section cannot cover all the possible combinations. So, to illustrate these aspects a quantification table was proposed.

The quantification of the influence was performed as follows (Table 3): if a parameter increase raised the IEI value, than the gained value is “+” while in the case of opposite impact (positive parameter increase, negative influence on the IEI value), the given value is “–”. Additionally, if no “reaction” was noticed in the IEI value during a structural parameter change or vice versa, the influence was considered 0.

4. Conclusions

In the present work it was shown that the build-up (synthesis pathway) of a catalyst cannot be neglected, due to the strong relationship between the structural features and degradation intermediates, which are extremely important if water purification is one of the target applications of these materials. It was demonstrated that by choosing the impregnation as the synthesis pathway for the P25/WO₃ composites, resulted in a material which contained the three WO₃ forms (amorphous, crystalline, doped) in different proportions. These forms manifested in different species (W⁶⁺, W⁴⁺, W_{def}), which influenced critically, the activity and the intermediate formation during the photodegradation. Furthermore, structural entities from the TiO₂ component were also influenced by the appearance of WO₃, such as the Ti³⁺. The appearance of gold in these material systems “disturbed” the “specie equilibrium” in the composites, resulting in the manipulation possibility of the previously mentioned structural particularities by simply changing the photodeposition wavelength of gold. Of course the trends and “links” observed here between the structure and IEI could easily change if the synthesis pathway is changed (Part II of the present work).

Acknowledgments

This work was supported for the Romanian authors by a grant of the Romanian National Authority for Scientific Research, CNCS–UEFISCDI, project number PN-II-ID-PCE-2011-3-0442. The Hungarian authors express their gratitude to the grant from Swiss Contribution (SH/7/2/20). Furthermore, the authors would express their gratitude to the funds received from contract MNT ERA.NET nr. 7-065/26.09.2012 and the Romanian-Hungarian bilateral project nr. 661/2013/K-TÉT_12.RO-1-2013-0109966.

Appendix A. Supplementary data

Supplementary data associated with this article can be found, in the online version, at <http://dx.doi.org/10.1016/j.apcatb.2013.09.019>.

References

- [1] D. Liu, F. Liu, J. Liu, *J. Power Sources* 213 (2012) 78–82.
- [2] L.M. Pastrana-Martinez, S. Morales-Torres, V. Likodimos, J.L. Figueiredo, J.L. Faria, P. Falaras, A.M.T. Silva, *Appl. Catal., B* 123 (2012) 241–256.
- [3] I. Tacchini, E. Terrado, A. Anson, M.T. Martinez, *Micro Nano Lett.* 6 (2011) 932–936.
- [4] K. Vinodgopal, I. Bedja, P.V. Kamat, *Chem. Mater.* 8 (1996) 2180–2187.
- [5] S.F. Chen, X.L. Yu, H.Y. Zhang, W. Liu, *J. Electrochem. Soc.* 157 (2010) K96–K102.
- [6] M.S. Hamdy, P. Nickels, I.H. Abd-Elmaksoud, H. Zhou, E.H. El-Mossalamy, A.O. Alyoubi, S. Lynch, A. Nathan, G. Thornton, *J. Photochem. Photobiol., A* 228 (2012) 1–7.
- [7] Y. Xie, S.H. Heo, Y.N. Kim, S.H. Yoo, S.O. Cho, *Nanotechnology* 21 (2010).
- [8] Y.K. Yuan, X.L. Xiao, Y.S. Wang, J.H. Xue, G.R. Li, R.H. Kang, J.Q. Zhang, L.F. Shi, *Sens. Actuators, B* 145 (2010) 348–354.
- [9] P.G. Su, L.N. Huang, *Sens. Actuators, B* 123 (2007) 501–507.
- [10] F.Z. Jia, Z.P. Yao, Z.H. Jiang, *Int. J. Hydrogen Energy* 37 (2012) 3048–3055.
- [11] Y.J. Zhang, W. Yan, Y.P. Wu, Z.H. Wang, *Mater. Lett.* 62 (2008) 3846–3848.
- [12] L. Xu, E.M.P. Steinmiller, S.E. Skrabalak, *J. Phys. Chem. C* 116 (2012) 871–877.
- [13] H.Y. Lin, C.Y. Kuo, *React. Kinet. Catal. Lett.* 94 (2008) 271–280.
- [14] E. García-Ramírez, M. Mondragon-Chaparro, O. Zelaya-Angel, *Appl. Phys. A–Mater. Sci. Process.* 108 (2012) 291–297.
- [15] D. Chen, H. Zhang, S. Hu, J.H. Li, *J. Phys. Chem. C* 112 (2008) 117–122.
- [16] H. Gomez, F. Orellana, H. Lizama, H.D. Mansilla, E.A. Dalchiele, *J. Chil. Chem. Soc.* 51 (2006) 1006–1009.
- [17] É. Karácsonyi, L. Baia, A. Dombi, V. Danciu, K. Mogyorósi, L.C. Pop, G. Kovács, V. Coșoveanu, A. Vulpoi, S. Simon, *Zs. Pap, Catal. Today* 208 (2013) 19–27.
- [18] R.Q. Cabrera, E.R. Latimer, A. Kafizas, C.S. Blackman, C.J. Carmalt, I.P. Parkin, *J. Photochem. Photobiol., A* 239 (2012) 60–64.
- [19] P.V. Kamat, *Abstr. Pap. Am. Chem. Soc.* (2007) 233.
- [20] V. Iliev, D. Tomova, L. Bilyarska, G. Tulyiliev, *J. Mol. Catal. A: Chem.* 263 (2007) 32–38.
- [21] M. Haruta, *Catal. Today* 36 (1997) 153–166.
- [22] A. Orlov, D. Jefferson, N. Macleod, R. Lambert, *Catal. Lett.* 92 (2004) 41–47.
- [23] V. Iliev, D. Tomova, L. Bilyarska, A. Eliyas, L. Petrov, *Appl. Catal., B* 63 (2006) 266–271.
- [24] U. Siemon, D. Bahnemann, J.J. Testa, D. Rodriguez, M.I. Litter, N. Bruno, *J. Photochem. Photobiol., A* 148 (2002) 247–255.
- [25] U.I. Gaya, A.H. Abdullah, *J. Photochem. Photobiol., C* 9 (2008) 1–12.
- [26] J.M. Herrmann, *Catal. Today* 53 (1999) 115–129.
- [27] G. Veréb, Z. Ambros, Zs. Pap, Á. Kmetykó, A. Dombi, V. Danciu, A. Cheesman, K. Mogyorósi, *Appl. Catal., A* 417–418 (2012) 26–36.
- [28] H. Zhang, J.F. Banfield, *J. Phys. Chem. B* 104 (2000) 3481–3487.
- [29] R. Jenkins, R.L. Snyder, *Introduction to X-ray Powder Diffractometry*, John Wiley & Sons, New York, 1996.
- [30] M. Baia, L. Baia, S. Astilean, *Chem. Phys. Lett.* 404 (2005) 3–8.
- [31] F. Toderas, M. Baia, L. Baia, S. Astilean, *Nanotechnology* 18 (2007) 255702.
- [32] D. Georgescu, L. Baia, O. Ersen, M. Baia, S. Simon, *J. Raman Spectrosc.* 43 (2012) 876–883.
- [33] L. Baia, A. Peter, V. Coșoveanu, E. Indrea, M. Baia, J. Popp, V. Danciu, *Thin Solid Films* 511–512 (2006) 512–516.
- [34] K.K. Akurati, A. Vital, J.-P. Delleman, K. Michalow, T. Graule, D. Ferri, A. Baiker, *Appl. Catal., B* 79 (2008) 53–62.
- [35] Z. Paszti, G. Petro, Z.E. Horvath, A. Karacs, L. Guczi, *Solid State Commun.* 107 (1998) 329–333.
- [36] T. Radu, D. Benea, R. Ciceo-Lucacel, O. Ponta, S. Simon, *J. Appl. Phys.* 111 (2012), art. no. 034701.
- [37] A.B. Boffa, H.C. Galloway, P.W. Jacobs, J.J. Benitez, J.D. Batteas, M. Salmeron, A.T. Bell, G.A. Somorjai, *Surf. Sci.* 326 (1995) 80–92.
- [38] M.S. Chen, W.T. Wallace, D. Kumar, Z. Yan, K.K. Gath, Y. Cai, Y. Kuroda, D.W. Goodman, *Surf. Sci.* 581 (2005) L115–L121.
- [39] J.T. Mayer, U. Diebold, T.E. Maday, E. Garfunkel, *J. Electron. Spectrosc. Relat. Phenom.* 73 (1995) 1–11.
- [40] D. Kumar, M.S. Chen, D.W. Goodman, *Thin Solid Films* 515 (2006) 1475–1479.
- [41] Zs. Pap, É. Karácsonyi, Z. Cegled, A. Dombi, V. Danciu, I.C. Popescu, L. Baia, A. Oszkó, K. Mogyorósi, *Appl. Catal., B* 111–112 (2012) 595–604.
- [42] D.M. Chen, G. Xu, L. Miao, L.H. Chen, S. Nakao, P. Jin, *J. Appl. Phys.* (2010) 107.
- [43] G. Leftheriotis, S. Papaefthimiou, P. Yianoulis, A. Siokou, *Thin Solid Films* 384 (2001) 298–306.
- [44] J. Riga, C. Tenret-Noël, J.J. Pireaux, R. Caudano, J.J. Verbist, Y. Gobillon, *Phys. Scr.* 16 (1977) 351–354.
- [45] A. Lehtonen, M. Wasberg, R. Sillanpää, *Polyhedron* 25 (2006) 767–775.